

Characterization of the Initial Stages of SBA-15 Synthesis by in Situ Time-Resolved Small-Angle X-ray Scattering

Andrei Y. Khodakov,^{*,†} Vladimir L. Zholobenko,[‡] Marianne Impérator-Clerc,[§] and Dominique Durand^{||}

Laboratoire de Catalyse de Lille, Université des Sciences et Technologies de Lille, Bât. C3, Cité Scientifique, 59655 Villeneuve d'Ascq, France, School of Chemistry and Physics, Keele University, Staffordshire ST5 5BG, United Kingdom, Laboratoire de Physique de Solides, UMR 8502, Bât. 510, Université Paris-Sud, 91405 Orsay Cedex, France, and Institut de Biochimie et de Biophysique Moléculaire et Cellulaire, Bât. 430, Université Paris-Sud, 91405 Orsay Cedex, France

Received: May 26, 2005; In Final Form: September 21, 2005

The initial stages of SBA-15 synthesis have been studied by using in situ time-resolved small-angle X-ray scattering with a synchrotron radiation source. The quantitative analysis of X-ray scattering and diffraction intensities allows the structures of intermediates to be identified at the different stages of SBA-15 synthesis. Following tetraethylorthosilicate (TEOS) addition, an intense small-angle scattering and an associated secondary maximum are observed, which are attributed to non-interacting surfactant template micelles encrusted with silicate species. After 25–30 min of the reaction, the broad scattering disappears and narrow Bragg diffraction peaks typical of hexagonally ordered structure are observed. The cylindrical micelles identified from X-ray scattering data appear to be the direct precursors of 2D hexagonal SBA-15 structure. Just after the formation of the SBA-15 hexagonal phase, the cylindrical micelles are only weakly linked in the hexagonal structure. As the synthesis proceeds, the solvent in the void volume between the cylindrical micelles is gradually replaced by more dense silicate species. The unit cell parameter of SBA-15 is progressively decreasing during the SBA-15 synthesis, which can be related to the condensation and densification of silicate fragments in the spaces between the cylinders. The volume fraction of the 2D hexagonally ordered phase is sharply growing during the first 2 h of the reaction. The inner core radius of SBA-15 material remains almost constant during the whole synthesis and is principally affected by the size of the poly(propylene oxide) inner core in the original cylindrical micelles.

1. Introduction

Novel mesostructured materials with adjustable porous networks have shown a great deal of promise for the design of new heterogeneous catalysts,^{1–4} semiconductors, low dielectric devices,⁵ and new separation processes.⁶ Therefore, their potential applications, synthesis, and characterization have been extensively investigated and reported.^{7–13} The most common 2D hexagonal type involves MCM-41^{10,14–18} and SBA-15.^{19–21} The mechanism of synthesis of mesoporous materials has been recently reviewed by Patarin et al.²² Synthesis of these siliceous mesoporous materials is similar in some ways to the procedures available for zeolites, requiring a silica source and a templating agent.²² Isomorphously substituted and composite materials can also be prepared using appropriate additives. However, in the synthesis of mesoporous materials, supramolecular assemblies of surfactant species act as the structure-directing agents.²² The reaction temperature is usually lower than that required for zeolite syntheses with many preparations carried out at 25–100 °C. When the solid structure is formed, the template molecules present in the channels can be removed by calcining

the sample or via solvent extraction.^{8,9,17} The pore diameter of a periodic solid can be controlled to a certain degree by choosing appropriate template and synthesis conditions. For the original M41S syntheses, two reaction pathways involving liquid crystal templating (LCT) have been proposed.^{14,15} The true LCT mechanism is based on the premise that the surfactant molecules organize independently of the inorganic silicate into a liquid crystal phase and the siliceous framework polymerizes around the preformed surfactant aggregates. According to the self-assembly mechanism, silicate anions in solution, being negatively charged species, play an intimate role in directing the formation of the supramolecular surfactant arrays. In both cases, the inorganic components (usually negatively charged at the high pH used) preferentially interact with the positively charged ammonium headgroups of the surfactants and are condensed into a solid. The resulting organic/inorganic mesostructure can be viewed as an array (e.g., hexagonal) of surfactant micelle rods embedded in a silica matrix. It is thought that the first mechanism does not operate for cationic surfactants because the surfactant concentrations used are below the critical concentration required for the liquid crystal phase formation. The second mechanism allows cooperative self-assembly of surfactant micelles and silicate precursor at much lower concentrations, and therefore, no preformed liquid crystal phase is necessary for the generation of mesostructured materials. The interplay between the two pathways depends on the surfactant properties, its concentration, and the ionic makeup of the

* Corresponding author. Phone: +33 3 20 33 54 37. Fax: +33 3 20 43 65 61. E-mail: andrei.khodakov@univ-lille1.fr.

† Université des Sciences et Technologies de Lille.

‡ Keele University.

§ Laboratoire de Physique de Solides, Université Paris-Sud.

|| Institut de Biochimie et de Biophysique Moléculaire et Cellulaire, Université Paris-Sud.

synthesis mixture.^{7,8,23,24} Further analysis of the self-assembly mechanism has been undertaken by Stucky and co-workers^{25–28} including the polydentate binding of silicate oligomeric species to the cationic surfactant, silicate polymerization in the interface region, and charge density matching between the silicate and the surfactant.

The important feature of the MCM-41 formation mechanisms is the interaction between cationic quaternary ammonium surfactants and anionic inorganic species ($S^{+}-I^{-}$) to produce two- or three-dimensional ordered structures. However, mesoporous materials can also be produced utilizing a range of electrostatic, covalent, van der Waals interaction, and hydrogen bonding (e.g., $S^{+}-X^{-}-I^{+}$, $S^{-}-M^{+}-I^{-}$, S^0-I^0 , etc.).^{19,20,26,29} In particular, the preparation of mesoporous silica employing nonionic surfactants has an advantage over the “electrostatic” route in the ease of surfactant removal by solvent extraction and the tendency to produce materials with thicker walls and a larger pore size. These materials of varying pore size can be synthesized from alkoxysilanes or from sodium silicate and a poly(ethylene glycol) ether neutral surfactant.^{19,20,30} For instance, SBA-15 type materials are synthesized in an acidic medium with poly(alkylene oxide) triblock copolymers such as Pluronic.^{19,20} The block copolymer molecules consist of hydrophobic and hydrophilic blocks.^{31–33} These molecules aggregate in aqueous solutions forming multimolecular aggregates having mostly spherical or cylindrical morphologies.³² In these aggregates, the hydrophobic blocks constitute the core and the hydrophilic blocks along with water compose the corona. Due to their larger pores (3–15 nm) and higher stability, SBA-15 materials are considered much more suitable than MCM-41 for a number of practical applications.^{4,19,20}

The pore diameter and the wall thickness are the major parameters, which influence possible utilization of mesoporous materials. Although it is known that the pore diameter in periodic mesoporous materials can vary from 2 to 30 nm, pore size tailoring of these materials appears to be a difficult task. Therefore, detailed information about the mechanism of the synthesis of mesoporous materials is indispensable for “tuning” the pore diameter and wall thickness in SBA-15 to the required values in a predefined range. Valuable structural information has been gained about ordered mesoporous materials using X-ray scattering, electron microscopy, and adsorption measurements, particularly from in situ investigation of the synthesis of mesoporous materials, including self-organization of organic and inorganic species, nucleation, and crystallization processes. Indeed, in situ X-ray diffraction (XRD) measurements have provided valuable insight into the formation of thin films of mesostructured materials,^{34–38} the transformation of hexagonal, lamellar, and cubic phases at elevated temperatures,^{39–45} and the development of periodic phases with d spacing values between 2 and 25 nm.^{46–50}

Small-angle X-ray scattering has been utilized as a powerful method for characterization of the structure of hexagonally ordered SBA-15 mesoporous materials.^{22,50–52} X-ray scattering could be very helpful in the identification of intermediates of SBA-15 synthesis present in the aqueous solutions and suspensions, while the position of Bragg diffraction peaks provides important information about the type of ordering and unit cell parameters in the ordered structures. The X-ray studies utilizing a synchrotron radiation source are well suited for in situ time-resolved measurements of the evolution of the ordered mesoporous phase in dilute synthesis mixtures, as the high brilliance of the synchrotron source allows fast acquisition of X-ray scattering patterns for the most demanding systems.

TABLE 1: Chemical Composition of Synthesis Mixtures

synthesis	concd HCl, g	TEOS, g	Pluronic, g	water, g
I	47.85	17.0	8.0	252.15
II	17.94	11.84	4	103.11

Our previous report⁵⁰ demonstrated the viability of the synchrotron based XRD method for characterization of synthesis mixtures for SBA-15 materials. It has been found that the unit cell of the forming SBA-15 materials is gradually contracting as the synthesis proceeds, which can be explained by the condensation reactions proceeding within the silicate walls of SBA-15. The XRD intensity values however are rather scattered, which has been attributed to the inhomogeneity of sampling from the reaction medium for XRD measurements. Since the XRD measurements have been delayed by the time required for sample collection and transfer from the synthesis mixture to the capillaries, very little information has been obtained about the first minutes of the SBA-15 synthesis. The initial stages of SBA-15 formation were also very recently studied by Flodström et al.⁵³ using in situ small-angle X-ray scattering. Flodström et al. suggested⁵³ that the formation of SBA-15 proceeded via clustering spherical P123 micelles. The cylindrical micelles were not detected in that work⁵³ at any stage of the synthesis. It appears, however, that some conclusions of their work regarding the structure of the intermediate species of SBA-15 synthesis may require further refinement.

The present work focuses on in situ characterization of the initial stages of SBA-15 synthesis by synchrotron based time-resolved X-ray scattering using a specially designed experimental setup. The detailed information about the intermediate structures was extracted from quantitative analysis of the small-angle scattering and diffraction intensities at different stages of SBA-15 synthesis. The results of this work are discussed together with the earlier data from the literature.

2. Experimental Section

The chemical composition of the two mixtures used for the synthesis of SBA-15 materials is shown in Table 1. In a typical SBA-15 synthesis,¹⁹ P123 block copolymer (poly(ethylene glycol)–poly(propylene glycol)–poly(ethylene glycol), average molecular mass 5800, Aldrich) was dissolved in a mixture of water and concentrated HCl under stirring. Tetraethylorthosilicate (TEOS) was the last component added to the synthesis mixture. The experimental setup used for the in situ X-ray scattering and XRD measurements is shown in Figure 1. The synthesis was carried out in a 250 mL glass flask, equipped with a magnetic stirrer, heated at 313 K. The synthesis mixture was circulating continuously through a 1.5 mm quartz capillary (wall thickness 0.01 mm). The circulation velocity was about 130 mL/min. To minimize any effects which might be due to possibly different flow characteristics during syntheses I and II, the diameter of the capillary, the geometry of the experimental cell, and the flow velocity were kept exactly the same during both syntheses.

The in situ small-angle X-ray scattering patterns were measured at the D43 experimental station at LURE, Orsay, France, using synchrotron radiation from the DCI storage ring running at 1.85 GeV with an average current of 250 mA. The D43 station utilized a single bent Ge monochromator (111) reflection, to select the wavelength and to focus the X-ray beam. The experimental setup was optimized for the measurements at small scattering angles bearing in mind large values of the

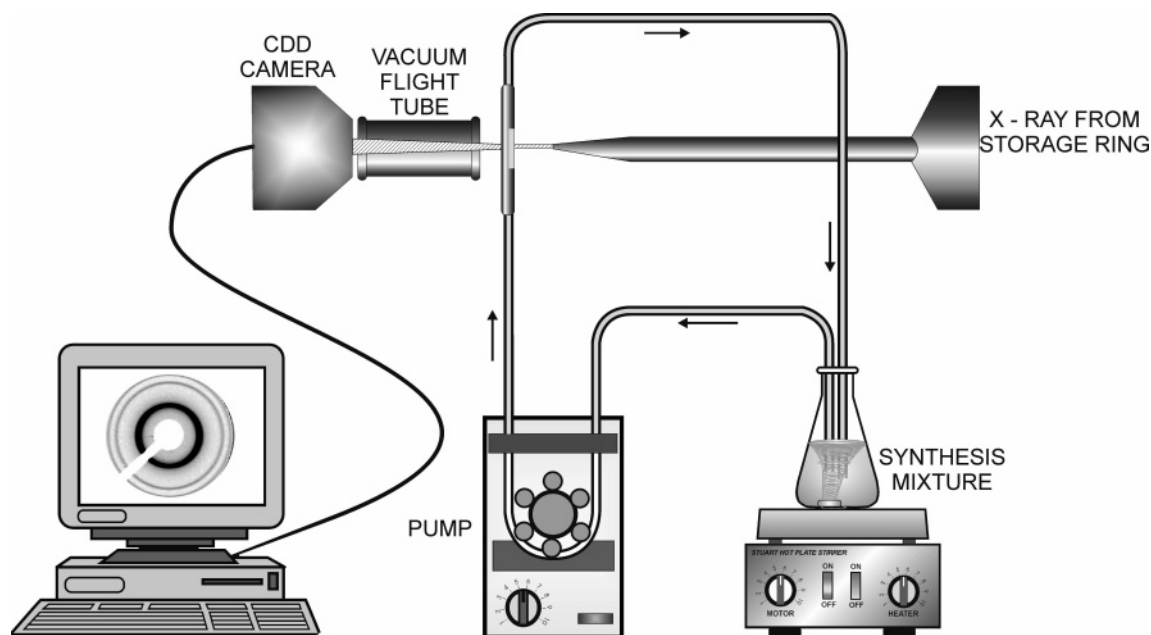


Figure 1. Experimental setup for in situ measurements of X-ray scattering and X-ray diffraction.

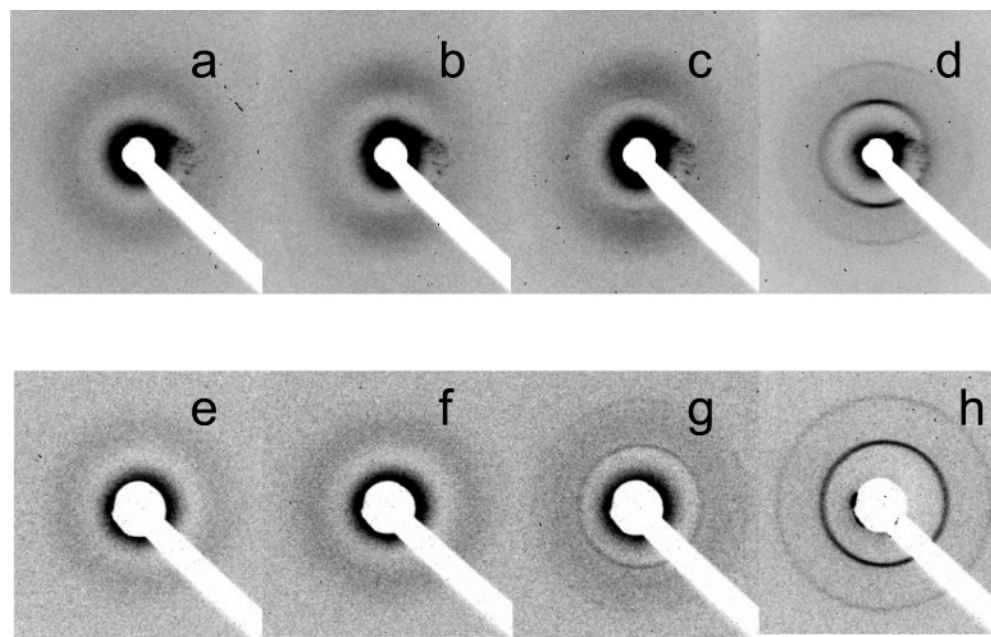


Figure 2. 2D X-ray scattering images measured after 15 (a), 20 (b), 25 (c), and 30 (d) min of synthesis I and after 15 (e), 20 (f), 25 (g), and 30 (h) min of synthesis II.

interplanar spacing in SBA-15 materials. The wavelength of the X-ray radiation was set to $\lambda = 0.1670$ (synthesis I) or 0.1449 nm (synthesis II), and the beam size was defined by a 0.5 mm diameter collimator. Vacuum flight tubes were placed between the sample and the detector to remove scattering and absorption of the X-ray beam by air.

The sample–detector distance was determined by calibration with silver behenate ($d_{001} = 5.838$ nm). The scattering patterns were recorded using the two-dimensional detector provided by the Laboratoire de Physique de Solides, Université Paris-Sud (CDD camera, Princeton Instruments). The spatial resolution (pixel size) of the detector was 0.054 mm. The scattering patterns were radially integrated, and the integrated intensity was plotted as a function of the scattering vector modulus $s = 2 \sin(\theta)/\lambda$, where 2θ is the scattering angle. The experimental

resolution was 0.0084 nm^{-1} (fwhm) for the s scale. The exposure times were typically 5 or 10 min for in situ measurements.

3. Results and Discussion

3.1. In Situ Time-Resolved X-ray Scattering Measurements. The in situ time-resolved 2D scattering image and integrated X-ray profiles of the synthesis mixtures I and II are presented in Figures 2–5. Very weak background X-ray scattering without any Bragg lines is observed prior to the addition of TEOS. After the addition of TEOS, an intense small-angle scattering along with an associated scattering ring are detected, with their intensity increasing during the first 20 min of the synthesis. The 2D X-ray scattering images (Figure 2b–d) measured at 20 – 25 min of synthesis I exhibit visible anisotropy, with the intensity of the scattering ring being higher

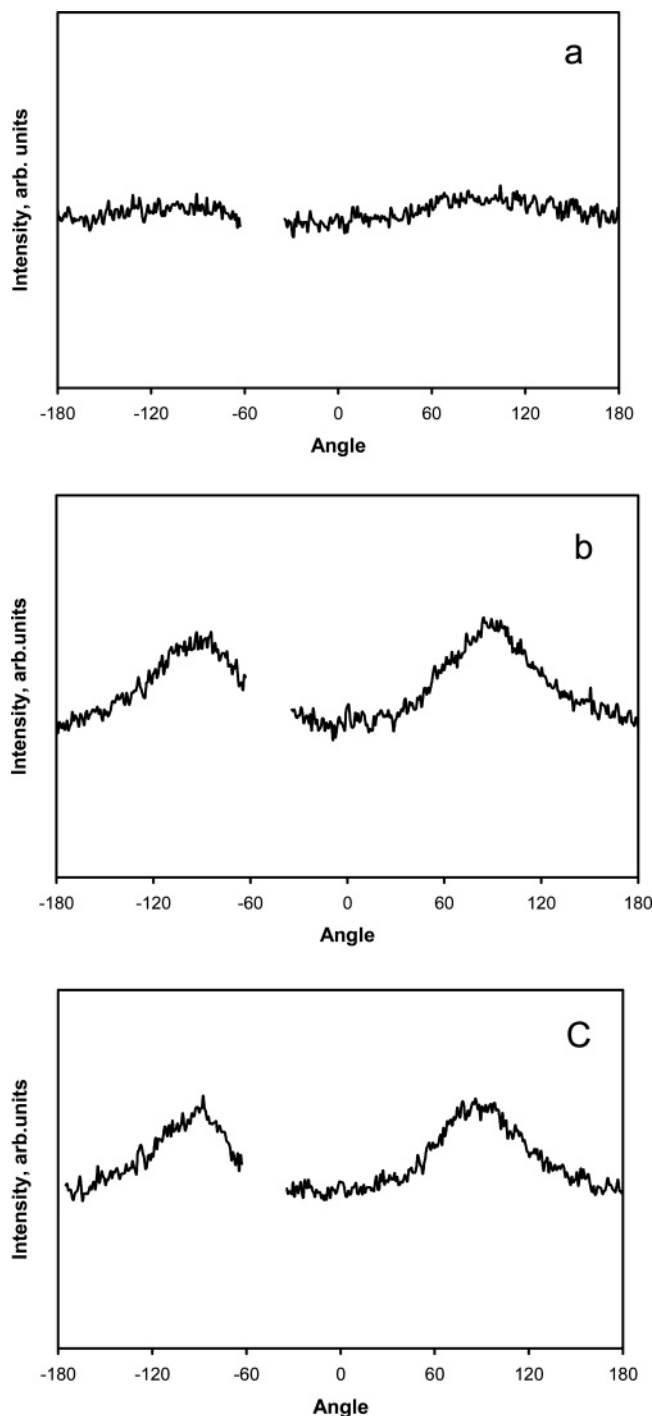


Figure 3. Profiles obtained by integrating the 2D scattering images measured after 15 (a), 20 (b), and 25 (c) min of synthesis I (Figure 2) along the scattering ring. The angles 0 and 90° correspond respectively to the equator and meridian of the scattering ring.

at the meridian than at the equator. The anisotropy is confirmed by the results of integration of the 2D images along the scattering ring (Figure 3). Taking into consideration the anisotropy of the 2D scattering images (Figures 2b–d and 3), the integration of scattering was carried out along a vertical line of 20 pixel width. Then the scattering profiles of the synthesis mixture prior to TEOS addition were subtracted from the patterns exhibiting broad scattering rings. The resulting scattering profiles for synthesis I are shown in Figure 4. No anisotropy in 2D scattering images was observed in synthesis II (Figure 2e–h). The scattering profiles (Figure 5) were obtained from the integration of full scattering images.

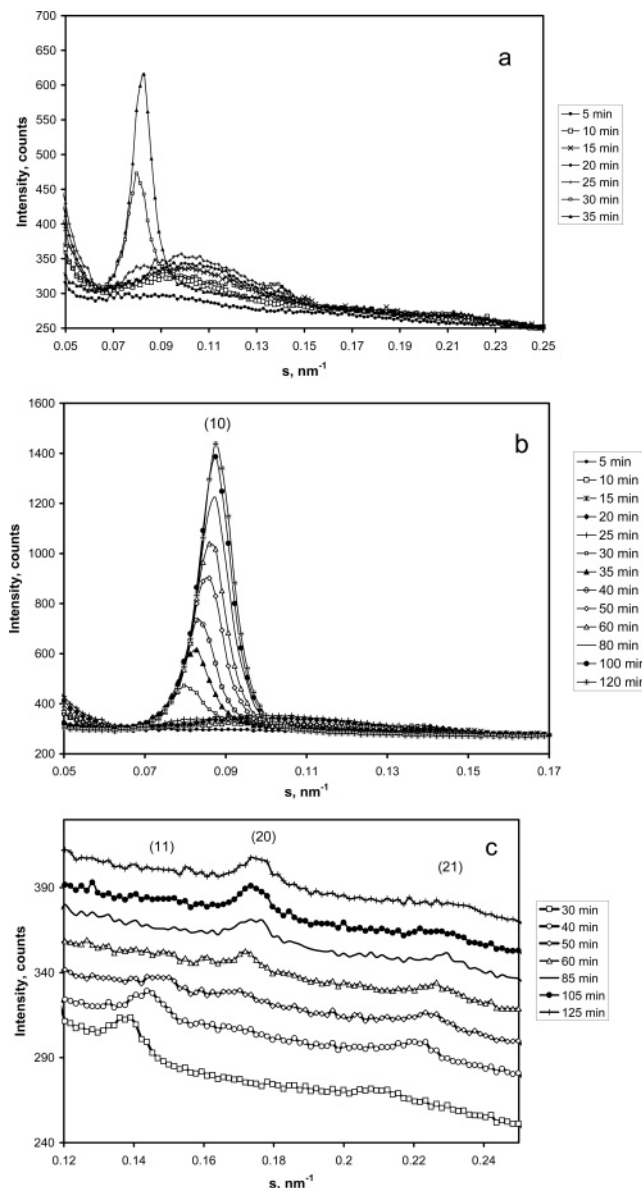


Figure 4. In situ time-resolved X-ray scattering profiles measured during synthesis I. The X-ray scattering profiles are offset in Figure 4c.

A similar broad scattering has been detected in previous reports^{47,53} during the initial stages of the formation of SBA-15 and MCM-41 materials and was attributed to the presence of micelles, which are supposed to be synthesis intermediates. The origin of the scattering observed at the initial stages of SBA-15 synthesis is discussed in more detail in section 3.2.

During the first 20 min, the solution has still been clear. After ~25 min of the synthesis, the solution becomes turbid; the solid precipitate is formed, and the X-ray patterns dramatically change (Figures 2, 4, and 5b,c). The intense small-angle scattering and broad scattering ring disappear, and the X-ray profiles characteristic of a 2D hexagonal structure are observed with up to four diffraction reflections, (10), (11), (20), and (21) detected for most samples. The width of the diffraction peaks is equal to the experimental resolution (0.0084 nm⁻¹). Therefore, the sizes of the 2D hexagonally ordered domains, which are produced in the early stages of the synthesis, are larger than 200 nm.

Figures 4 and 5 show that, as the reaction proceeds, the (10), (11), (20), and (21) diffraction peaks are shifting to higher s

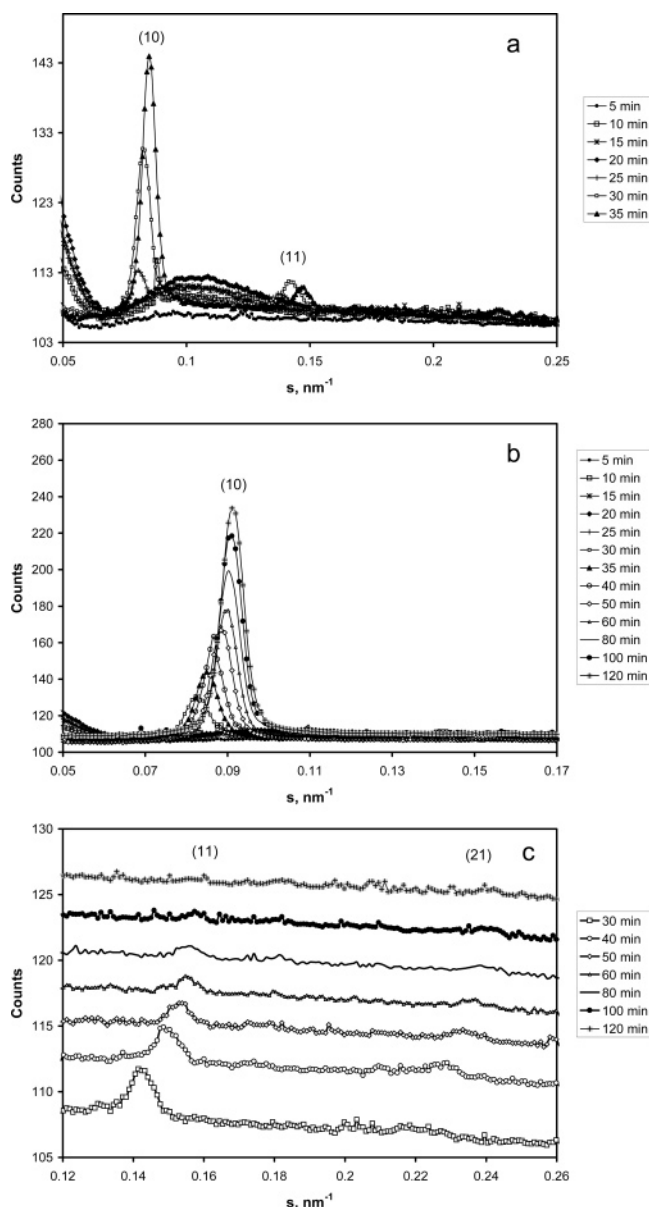


Figure 5. In situ time-resolved X-ray scattering profiles measured during synthesis II. The X-ray scattering profiles are offset in Figure 5c.

values. They indicate a decrease in the d_{10} , d_{11} , and d_{20} spacings and in the unit cell parameter, a , which can be calculated from the position of the (10) diffraction line using the equation

$$a = \frac{2}{\sqrt{3}}d_{10}$$

Our data show a steady decrease in the calculated unit cell parameter, a , of the hexagonal lattice for both preparations during the first 2 h of the synthesis. This observation is consistent with earlier reports,^{50,53} and such a decrease in the hexagonal unit cell parameter during SBA-15 synthesis can be explained by the condensation reactions within silicate walls.^{21,48,49}

For both syntheses, the intensity of the (10) reflection is increasing during the first hours of the reaction, while the intensities of the (11) and (21) reflections are decreasing. The behavior of the (20) reflection intensity is somewhat more complex. In the early stages of synthesis I, the (20) reflection is not observed; it can be seen only after 40 min of the reaction

(Figure 4c). During synthesis II (Figure 5c), the (20) diffraction reflection has not been detected.

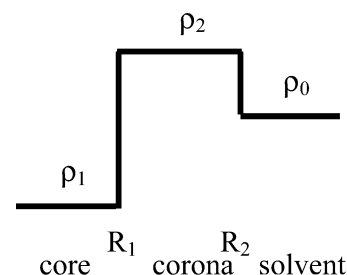
The obtained in situ X-ray time-resolved results reveal the presence of two different steps of SBA-15 synthesis: the first step is characterized by the broad X-ray scattering signals and the second by the Bragg diffraction peaks. The sections below address the determination of the structures of the synthesis intermediates associated with these two steps, using the original method of quantitative analysis of X-ray scattering and X-ray diffraction intensities.

3.2. Characterization of the Intermediates of SBA-15 Synthesis using X-ray Scattering. Before discussing X-ray scattering data, some basic equations should be briefly reviewed.^{54,55} The intensity of X-ray scattering over identical micelles in the solution is expressed by

$$I(s) = F(s) S(s) \quad (1)$$

where $F(s)$ is the form factor, $S(s)$ is the structure factor, and s is the modulus of scattering vector. The structure factor is due to the interactions between the micelles and could produce a peak of intermicelle correlation in the scattering patterns. If the interaction between the micelles is negligible, the scattering intensity, $I(s)$, is equal to the form factor, $F(s)$.

In agreement with previous reports,^{31–33} we suggest that, in the micelles originating from dissolution of P123 block polymer in aqueous solutions, the poly(propylene oxide) (PPO) hydrophobic block with electron density ρ_1 constitutes the inner core and the poly(ethylene oxide) (PEO) hydrophilic block along with water molecules and eventually silicate species (after TEOS addition) with electron density ρ_2 form the corona. These micelles are free to move inside the aqueous solution of hydrochloric acid with electron density ρ_0 .



The electron density was estimated from the known electronic structure and volumetric density of the substances considered in the present study. The electron densities of the aqueous solution of hydrochloric acid and the PPO core of micelles are respectively $\rho_0 \approx 0.35 \text{ e}/\text{\AA}^3$ and $\rho_1 \approx 0.33 \text{ e}/\text{\AA}^3$. The electron density of the PEO corona, ρ_2 , is about $0.36 \text{ e}/\text{\AA}^3$, taking into account its hydration (0.37 for pure PEO).³²

Previous reports^{32,53,56} suggest that the micelles forming from P123 Pluronic block polymer in aqueous solution might have spherical or cylindrical morphologies. Below are some equations describing X-ray scattering on spherical or cylindrical micelles.^{54,55}

Spherical Micelles. The intensity of scattering can be presented as

$$I(s) = n_s \left(\frac{4}{3} \pi \right)^2 [(\rho_2 - \rho_0) \Phi(2\pi s R_2) R_2^3 + (\rho_1 - \rho_2) \Phi(2\pi s R_1) R_1^3]^2 \quad (2)$$

where n_s is the number of the spherical micelles, R_2 is the external micelle radius, and R_1 is the radius of the PPO inner

core. The function Φ is given by

$$\Phi(2\pi sR) = 3 \frac{\sin(2\pi sR) - 2\pi sR \cos(2\pi sR)}{(2\pi sR)^3}$$

After denoting $\beta = (\rho_2 - \rho_1)/(\rho_2 - \rho_0)$, eq 1 can be rewritten in the form

$$I(s) = n_s \left(\frac{4}{3}\pi \right)^2 (\rho_2 - \rho_0)^2 R_2^6 \left[\Phi(2\pi sR_2) - \beta \frac{R_1^3}{R_2^3} \Phi(2\pi sR_1) \right]^2 \quad (3)$$

Cylindrical Micelles. Provided that the length of the cylindrical micelles is $L \gg 1/s$, the scattering intensity is defined by the following equation

$$I(s) = n_s \frac{1}{s} 4\pi (\rho_2 - \rho_0)^2 L R_2^4 \left[\frac{J_1(2\pi sR_2)}{2\pi sR_2} - \beta \frac{R_1^2}{R_2^2} \frac{J_1(2\pi sR_1)}{2\pi sR_1} \right]^2 \quad (4)$$

where n_s is the number of cylindrical micelles in the solution, R_1 and R_2 are respectively the radii of the inner core and micelle corona, and $J_1(2\pi sR)$ is the Bessel function of order 1.

The experimental in situ time-resolved X-ray scattering profiles of syntheses I and II are presented in Figures 4 and 5. First, we will discuss the data obtained for synthesis I.

A very weak and flat X-ray scattering without any Bragg lines is observed in synthesis I prior to the addition of TEOS. The very low intensity of X-ray scattering prior to the addition of TEOS is consistent with the presence in the solution of hydrochloric acid of either spherical or cylindrical micelles constituted by the PPO core and PEO corona. Indeed, whatever the shape of micelles, the scattering intensity (eqs 3 and 4) depends on the disparity of electron density between the micelle core, corona, and solvent. The corona and solvent are expected to have very similar electron densities ($\rho_0 \approx 0.35 \text{ e}/\text{\AA}^3$ and $\rho_2 \approx 0.36 \text{ e}/\text{\AA}^3$). The contrast with the core ($\rho_1 \approx 0.33 \text{ e}/\text{\AA}^3$) appears to also be too small to yield any detectable signal.

A broad scattering ring along with an intense small-angle scattering can be seen after 5, 10, 15, 20, and 25 min of synthesis I (Figures 2a–d and 4). This scattering disappears completely after 30 min of the reaction, and the Bragg reflections characteristic of the 2D hexagonal phase can be observed. After 25 min of synthesis I, the intense small-angle scattering and scattering ring coexist with the already generated Bragg diffraction reflections of the 2D hexagonal phase.

The presence of the broad scattering ring during the first minutes of synthesis I can be interpreted in two ways: First, this ring can be related to the correlation between scattering objects or, in other words, to a maximum of the structure factor, $S(s)$ (eq 1). Second, the broad scattering ring can be attributed to the first secondary maximum of the form factor, $F(s)$, for a system of identical spherical or cylindrical micelles without any correlation.

A more detailed analysis, however, suggests that the broad X-ray scattering ring observed at the early stages of synthesis I is more likely to be attributed to the X-ray scattering over independent identical particles rather than to the short-distance correlation. Indeed, if the broad peak located at $s_m \approx 0.1 \text{ nm}^{-1}$ were related to the short-distance correlation, this would give an average micelle–micelle distance $d \approx 1.23/s_m \approx 12\text{--}12.5 \text{ nm}$ shorter than the lattice parameter, a , in the 2D hexagonally ordered solid materials ($a \approx 14.3 \text{ nm}$ at 25 min synthesis time)

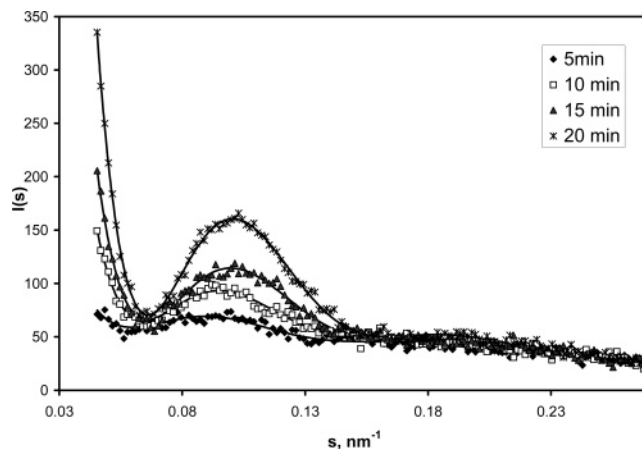


Figure 6. Fits of X-ray scattering profiles observed during the initial stages of synthesis I using the model of cylindrical micelles.

(Figure 4a,b). The appearance of a broad scattering peak at 0.1 nm^{-1} during the first minutes of synthesis I is accompanied by an increase in the intensity of X-ray scattering at very small angles ($<0.6 \text{ nm}^{-1}$). This observation seems to be in favor of attribution of the broad peak to the scattering from independent particles. Therefore, it is suggested that the broad peak at 0.1 nm^{-1} might be attributed to the first secondary maximum of X-ray scattering over non-interacting micelles.

The scattering images obtained after 20 and 25 min of synthesis I exhibit noticeable anisotropy (Figures 2b–d and 3). The anisotropy of 2D scattering images suggests the alignment of the micelles along the flow in the capillary used in the experimental setup (Figure 1) for measuring X-ray scattering. The anisotropy of the scattering also suggests that the micelles are nonspherical after the TEOS addition. This suggestion is consistent with earlier works. It was shown, for example,³² that the micelles of Pluronic polymers could be cylindrical or spherical in aqueous solutions. The observed X-ray scattering profiles after subtraction of the background were fitted using the model of cylindrical micelles (eq 4). The background scattering was approximated by a straight line. Figure 6 shows that the fits using eq 4 are all of excellent quality even at very low s . The results (Table 2) suggest, therefore, that the cylindrical micelles could form at the very beginning of synthesis I and their structure (β , R_1 , and R_2 parameters) evolves only very slightly with time.

Assuming the electron densities of the micelle core ($\rho_1 = \rho_{\text{PPO}} = 0.33 \text{ e}/\text{\AA}^3$) and the solvent ($\rho_0 = \rho_{\text{solvent}} = 0.35 \text{ e}/\text{\AA}^3$) are close to the known values, the value $\beta = 1.22$ evaluated from the fits corresponds to an electron density of the cylinder corona of $\rho_2 = 0.44 \text{ e}/\text{\AA}^3$. Thus, the electron density of the cylinder corona increases after the addition of TEOS from a value of $\rho_{\text{PEO}} = 0.36 \text{ e}/\text{\AA}^3$ in the initial PEO block to a value of $0.44 \text{ e}/\text{\AA}^3$ after TEOS addition. The increase in the electron density in the cylinder shell, ρ_2 , could be attributed to the diffusion of TEOS molecules from the solution of hydrochloric acid to the hydrophilic PEO layer and their subsequent hydrolysis. Thus, the silicate species released on TEOS hydrolysis densify the cylinder shells and, thus, increase the electron density. The densification of the micelle corona also increases the intensity of X-ray scattering after TEOS addition relative to the scattering on the original Pluronic PPO–PEO micelles. The radii of the inner core and whole micelle evaluated from eq 4 were respectively about 4 and 7 nm (Table 1). These values are close to the previously calculated dimensions of P123 Pluronic cylindrical micelles in aqueous solutions. The calculations³² using a simple molecular theory of solubilization yield

TABLE 2: Fits of the Experimental Scattering Profiles and Bragg Intensities Observed during Synthesis I^a

time, min	I_{10} , arb units	$(I_{11}/I_{10})10000$ (sign(F_{11}/F_{10}))		$(I_{20}/I_{10})10000$ (sign(F_{20}/F_{10}))		$(I_{21}/I_{10})10000$ (sign(F_{21}/F_{10}))		a , nm	R_1	R_2	β
		exptl	calcd	exptl	calcd	exptl	calcd				
5				cylindrical micelles					4.8	7.1	1.21
10				cylindrical micelles					3.94	7.37	1.19
15				cylindrical micelles					3.91	6.96	1.22
20				cylindrical micelles					3.79	7.01	1.22
30	1.84	1000	1000 (+)	0	1 (−)	818	819 (−)	14.49	4.1	6.66	1.927
35	3.62	650	650 (+)	0	0 (+)	575	574 (−)	13.94	3.9	6.23	2.679
40	5	327	327 (+)	10	0 (−)	389	389 (−)	13.94	3.96	6.44	3.38
45	6.04	147	147 (+)	53	54 (−)	279	281 (−)	13.68	3.98	6.63	3.777
50	6.98	99	99 (+)	71	71 (−)	247	246 (−)	13.43	3.95	6.6	4.04
55	7.76	57	57 (+)	155	155 (−)	274	273 (−)	13.43	4.18	6.51	2.89
60	8.41	21	21 (+)	106	106 (−)	150	151 (−)	13.43	4.02	6.97	5.711
85	10.6	0	16 (−)	159	145 (−)	123	91 (−)	13.20	4.2		
105	12.2	0	13 (−)	148	140 (−)	105	95 (−)	13.20	4.18		
125	13.05	0	13 (−)	146	141 (−)	83	94 (−)	13.20	4.18		
150	12.6	0	2 (−)	142	142 (−)	90	92 (−)	13.13	4.15		

^a For reaction times less than 25 min, the scattering profiles were fitted using the model of cylindrical micelles; fits of the Bragg peak intensities were performed using the model of a hexagonal phase. The signs of the calculated diffraction amplitudes are given, where $I_{hk} = |F_{hk}|^2$.

TABLE 3: Fits of the Experimental Scattering Profiles and Bragg Intensities Observed during Synthesis II (the Notation Is the Same as That in Table 2)

time, min	I_{10} , arb units	$I_{11}/I_{10}(10000)$ (sign(F_{11}/F_{10}))		$I_{20}/I_{10}(10000)$ (sign(F_{20}/F_{10}))		$I_{21}/I_{10}(10000)$ (sign(F_{21}/F_{10}))		a , nm	R_1 , nm	R_2 , nm	β
		exptl	calcd	exptl	calcd	exptl	calcd				
20				cylindrical micelles					3.26	7.0	1.10
30	1.89	1618		0		0		14.05			
35	2.76	871	871 (+)	0	4 (+)	1036	1038 (−)	13.62	4.22	5.32	1.65
40	3.73	575	574 (+)	0	3 (+)	514	517 (−)	13.33	3.73	5.69	3.03
45	3.76	360	360 (+)	0	2 (+)	303	305 (−)	13.20	3.59	5.57	5.18
50	4.05	280	280 (+)	0	0 (+)	168	168 (−)	12.97	3.37	6.43	9.04
55	4.51	229	229 (+)	0	0 (+)	150	150 (−)	12.93	3.37	6.55	12.16
60	5.05	145	145 (+)	0	0 (−)	141	136 (−)	12.83	3.4		
80	6.69	85	86 (+)	0	6 (−)	156	146 (−)	12.80	3.51		

for the cylindrical P123 micelles in aqueous solutions a radius of the inner PPO block of 4.2 nm and a radius of the whole micelles of 6.6 nm.

An attempt was also made to fit the scattering patterns obtained during the first 30 min of synthesis I using the model based on spherical micelles (eq 3). The fitting, however, produces incoherent parameters for the scattering profiles observed after 10, 15, and 20 min of the reaction. The values of R_1 obtained from the fit were between 2.39 and 4.3 nm, and the values of R_2 were 8.4–8.9 nm with $\beta = 2.15$ –8.44. A value of β higher than 2 gives the electron density of the micelle corona after the addition of TEOS, ρ_2 , close to that of initial PEO (0.353–0.367 e/Å³). Note that no X-ray scattering should be observed under these conditions, since the electron density of the micelle corona, ρ_2 , would be very close to the electron density of the HCl solution, ρ_0 (eq 3). Note, however, that the fitting of scattering patterns with spherical micelles at 5 min of synthesis I yields values of $\beta = 1.2$ with $R_1 = 6.5$ nm and $R_2 = 7.5$ nm. $\beta = 1.2$ corresponds to a value of $\rho_2 = 0.44$, that is, to the corona of spherical micelles containing dense silicate species. Therefore, the presence of spherical micelles cannot be ruled out prior to TEOS addition and after 5 min of synthesis I. The spherical shape of P123 micelles in aqueous solutions of hydrochloric acid prior to TEOS addition is consistent with previous neutron scattering data.⁵⁷ Our X-ray scattering data show however that if even the spherical micelles were present prior to TEOS addition and during the first 5 min of synthesis I, in the presence of TEOS after 10 min of the reaction, all of them would adopt a cylindrical shape.

For synthesis II, the data are qualitatively similar to those of synthesis I. No measurable X-ray scattering was observed prior

to TEOS addition. An intense central scattering spot together with first secondary maxima are detected during the first 25 min of the reaction (Figures 2e–h and 5). Then, the intensity of the broad scattering ring drops sharply and the Bragg diffraction lines of the 2D hexagonal phase are observed. In contrast to synthesis I, no anisotropy of the scattering image was observed during the first minutes of the reaction. For the scattering profile obtained after 20 min of synthesis II, the model of cylindrical micelles yields fitting of good quality with the parameters (Table 3), which only slightly differ from those of synthesis I (Table 2). A β value of 1.10 corresponds to an electron density in the micelle corona of $\rho_2 = 0.55$ e/Å³, which is a little higher than that in synthesis I and is consistent with the higher concentration of TEOS involved in synthesis II than in synthesis I. On the contrary, the fitting of scattering profiles with cylindrical micelles observed at 5, 10, and 15 min of synthesis II leads to a β parameter lower than 1. $\beta < 1$ corresponds to the situation where the electron density of the solvent is lower than the electron density of the micelle inner core ($\rho_0 < \rho_1$), which is incompatible with the known values of the electronic density of PPO (0.33 e/Å³) and solution of hydrochloric acid (0.35 e/Å³). This suggests that the model of cylindrical micelles does not provide an adequate representation of the X-ray scattering profiles at reaction times smaller than 20 min. That was the reason why the model of spherical micelles was also used to fit the scattering data obtained during synthesis II after 5–20 min of the reaction.

The results obtained for synthesis II using the model of spherical micelles are presented in Table 4. First, we tried to fit with spheres the scattering profiles obtained after 20 min of the reaction. For the data at 20 min, the fitting yields the

TABLE 4: Fits of Experimental Scattering Intensities at the Initial Stages of Synthesis II Using the Model of Spherical Micelles

time, min	R_1 , nm	R_2 , nm	β
5	6.3	7.0	1.10
10	4.7	8.18	1.32
15	4.59	8.24	1.31
20	2.36	8.46	5.8

parameter $\beta \approx 5.8$ which corresponds to an electron density in the micelle corona, ρ_2 , that is too close to the density of HCl solution, ρ_0 . When the electron density of the corona is very close to the density of the solution (eq 3), the intensity of X-ray scattering on the micelle corona should be very low. This seems to confirm the suggestion that after 20 min of the reaction just prior to the appearance of the 2D hexagonal phase, the synthesis mixture does not contain spherical micelles but consists of mostly cylindrical ones. Note, however, that, similar to synthesis I, the fit using the model of spherical micelles gives reasonable values of $\beta = 1.1$ and $R_1 = 6.3$ nm and $R_2 = 7.0$ nm after 5 min of the reaction. This suggests that, as it was with synthesis I, identical spherical micelles are present during the first 5 min of synthesis II. The model based on the assumption of identical spherical micelles does not provide, however, an adequate description of the micelles after 10 and 15 min of the synthesis. Table 4 shows that the parameter β slightly increases as the synthesis progresses. The increase in the β parameter is not consistent with an increase in the electron density in the corona and consequently with the suggested mechanism of the synthesis, which involves gradual enrichment of the PEO corona with silicate ions after TEOS addition.

Thus, both models based on the assumption of identical cylindrical or spherical micelles fail to provide the appropriate description of the micelle structure after 10–15 min of synthesis II. It can be suggested therefore that at this stage that the system appears to be much more complex than that of synthesis I. It may consist of spherical and cylindrical micelles of different sizes. The presence of micelles of different geometries during the first minutes of synthesis II could explain the absence of anisotropy in the 2D scattering images (Figure 2e–h). This would also certainly make it difficult to model the scattering profiles at this stage of the synthesis.

Interestingly, in syntheses I and II, the modeling strongly indicates that the cylindrical micelles precede the appearance of the 2D hexagonal phase. This suggests the crucial role that the cylindrical micelles could play in the mechanism of SBA-15 synthesis.

3.3. Analysis of Bragg Diffraction Intensities. The structure of the 2D hexagonal phase at the second stage of SBA-15 synthesis has been analyzed in a more quantitative manner using the intensities of the (10), (11), (20), and (21) Bragg diffraction lines. First, we will recall the model used for the analysis of XRD reflection intensities in our earlier work.⁵¹ For a 2D hexagonal structure,^{51,52} the diffraction intensity associated with the line of indexes (h, k) is given by

$$I(s) = KM(h, k) \frac{|A(s)|^2}{s^2} \phi \quad (5)$$

The scattering vector modulus, s , is a function of indexes (h, k)

$$s = \frac{2}{\sqrt{3}a} \sqrt{h^2 + k^2 + hk} \quad (6)$$

where a is the lattice parameter of the 2D hexagonal structure. $A(s)$ represents the structure factor that is the Fourier transform of the electronic density in the unit cell. $1/s^2$ is the Lorentz factor at small angles for powder,⁵⁸ and $M(h, k)$ is the line multiplicity; ϕ is the volume fraction of the hexagonal SBA-15 phase. The line multiplicities in the 2D hexagonal lattice were respectively 6 for the lines (10), (11), (20), and (30) and 12 for the line (21). K is a multiplicative constant related to the X-ray beam intensity and sample volume, assuming a constant absorption by the sample.

First, the simple model, which assumes the presence of a two-dimensional assembly of cylinders embedded in a uniform silica matrix was used to simulate the diffraction intensities.⁵¹ The two-level model suggests the presence of two regions of electron density, that is, a two-level approach. The electron density in the present model is described by a step change between the core and silica matrix. The intensity is calculated as

$$I(s) = \frac{R^4}{(sa)^2} KM(h, k) (\rho_2 - \rho_1)^2 \left[\frac{J_1(2\pi s R)}{2\pi s R} \right]^2 \phi \quad (7)$$

where R is the core radius, ρ_1 and ρ_2 are electronic densities in the cylinder core and silica matrix, and J_1 is the Bessel function of order 1.

At the very beginning, the observed intensities of the Bragg peaks cannot be described using the two-density-level model. In agreement with our previous work,⁵¹ a more realistic model, which takes into consideration the presence of three regions of electron density, was used for the quantitative description of XRD data. This model is consistent with the description of the first stage of the synthesis using the model of cylindrical micelles (section 3.2). In the three-level model, the first region of electron density represents the inner core of the cylinders filled by PPO species (electron density ρ_1), the second region corresponds to the cylinder corona formed by the mixture of silicate and PEO species with electron density ρ_2 , and the third region with electron density ρ_0 is constituted by the spaces between the cylinders. The intensity of the diffraction lines is given by the following formula:

$$I(s) = \frac{R_2^4}{(sa)^2} KM(h, k) (\rho_2 - \rho_0)^2 \left[\frac{J_1(2\pi s R_2)}{2\pi s R_2} - \beta \frac{R_1^2}{R_2^2} \frac{J_1(2\pi s R_1)}{2\pi s R_1} \right]^2 \phi \quad (8)$$

where R_1 and R_2 are respectively the radii of the inner core and the whole cylinder. The electron densities affect the XRD intensities through the ratio $\beta = (\rho_2 - \rho_1)/(\rho_2 - \rho_0)$. The fit parameters of this model are only R_1 , R_2 , and β . Note that ρ_2 , ρ_0 , and ϕ enter only in the prefactor, which is normalized during the fitting. From eq 8, one can also calculate the signs of the diffraction amplitudes, which are given by the sign of the expression in square brackets $[(J_1(2\pi s R_2)/2\pi s R_2) - (\beta R_1^2/R_2^2) \cdot (J_1(2\pi s R_1)/2\pi s R_1)]$, taking into account the values of the parameters (R_1 , R_2 , and β) determined by the fitting procedure.

The results of the fits along with the signs of the diffraction amplitudes for syntheses I and II are shown in Tables 2 and 3. The three-level model (eq 8) represents satisfactorily the XRD data obtained during the first hour of the synthesis. After 60 min of synthesis, this model transforms into the model based on the two density levels (eq 7). The model based on two density levels corresponds to the situation in the three-density-level model where ρ_2 is equal to ρ_0 . Consequently, eq 8 reduces to

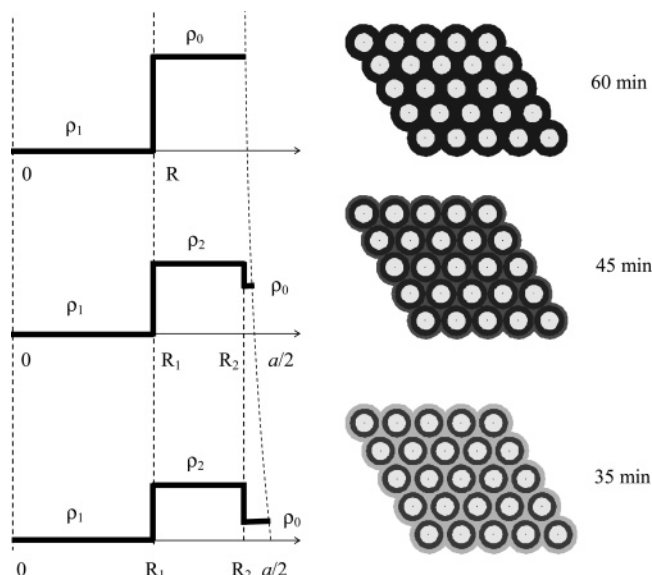


Figure 7. Formation of 2D hexagonal SBA-15 structure from cylindrical polymer-silicate micelles.

eq 7. It can be suggested, therefore, that, after 60 min of synthesis, the electron density of the cylinder corona becomes close to the electron density in the spaces between the cylinders. The observed phenomenon is likely to be attributed to the densification of the spaces between the cylinders due to silica condensation. Tables 2 and 3 display a monotonic increase in the β parameter during the first hour of the synthesis. Assuming an electron density in the inner core of the cylinders close to that in PPO ($\rho_1 = 0.33 \text{ e}/\text{\AA}^3$) and an electron density in the cylinder corona in hexagonal structure close to the value determined for cylindrical micelles from X-ray scattering ($\rho_2 = 0.44$ in synthesis I and $0.55 \text{ e}/\text{\AA}^3$ in synthesis II), the increase in the β parameter would correspond to the increase in the electron density in the inter-cylinder gaps, ρ_0 , from its initial value in the solution of hydrochloric acid ($0.35 \text{ e}/\text{\AA}^3$) up to the electron density in the corona. The mechanism of packing cylindrical micelles into 2D hexagonal structure is schematically presented in Figure 7. During the first 20 min after TEOS addition, the Pluronic micelles represent almost independent objects in the solution of hydrochloric acid. After 25 min, these micelles start packing into 2D hexagonal structure. At the beginning, the cylinders are only weakly linked via their coronas in the 2D hexagonal matrix. As the synthesis proceeds, the spaces between the cylinders are gradually filled by the silicate species. After 1 h of the reaction, the density in the spaces between the cylinders is getting very close to the electron density in the micelle corona.

The evolution of the hexagonal unit cell parameter, a , calculated radii of the inner core, R_1 , and whole cylinder, R_2 , during the second step of SBA-15 synthesis is shown in Figure 8. The hexagonal unit cell parameter, a , shows continuous decrease during the synthesis. Despite significant changes in the ratio of diffraction intensities, the radius of the cylinder inner core, R_1 , only slightly fluctuates during the SBA-15 synthesis. This observation is in accordance with the self-assembly mechanism, in which the formation of the ordered mesophase is initiated by the added silicate species. Moreover, the fact that the lattice parameter, a , is almost equal to $2R_2$ is also in agreement with this mechanism.

3.4. Initial Stages of SBA-15 Synthesis. In summary, the analysis of the X-ray scattering data suggests that, during the first 5 min of the reaction, the PPO-PEO micelles might have

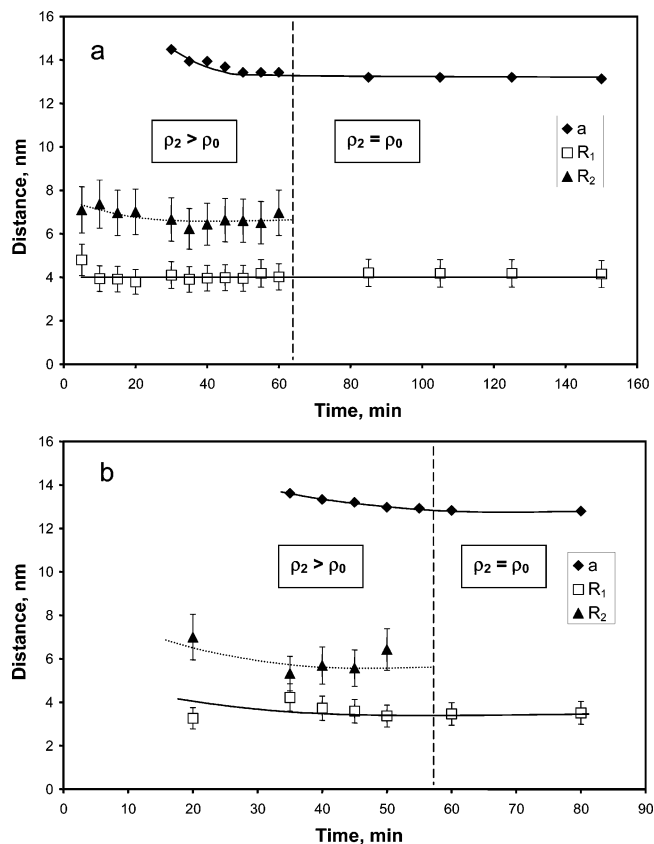


Figure 8. Evolution of the structural parameters of the 2D hexagonal phase during SBA-15 synthesis: (a) synthesis I; (b) synthesis II.

a spherical shape. In the presence of silicate species generated via TEOS hydrolysis in both synthesis I and synthesis II, most of micelles adopt the cylindrical shape. For synthesis I, the conversion to the cylindrical shape seems to proceed more swiftly than that for synthesis II. These cylindrically shaped micelles are then packing in 2D hexagonal structure yielding SBA-15 materials. Overall, within the accuracy of the model, the diameter of inner core of the SBA-15 mesoporous materials prepared at lower temperatures appears to be principally determined by the diameter of the PPO core in the surfactant-silicate cylindrical micelles. In the present work, the analysis of scattering patterns after 10–20 min of syntheses I and II clearly indicates that a solution of non-interacting cylindrical micelles precedes the appearance of the 2D hexagonal phase. The presence of cylindrical micelles is also proved by the anisotropy of scattering images observed after 20–25 min of synthesis I. The solution was limpid before the appearance of the 2D hexagonal phase, and no peak of intermicelle correlation was observed. This suggests that the micelles could be considered as non-interacting objects during 20–25 min of the synthesis and their aggregation immediately results in the formation of the 2D hexagonal phase detectable by intense XRD patterns.

In very recent papers by Flodström et al.,^{53,56} X-ray scattering and electron microscopy were used to study the different intermediates during the initial stages of SBA-15 synthesis. In contrast to the publication by Flodström et al.,⁵³ we propose a mechanism of formation of SBA-15 materials based on the non-interacting cylindrical micelles. In the previous report by Flodström et al.,⁵³ the synthesis of SBA-15 materials was suggested to proceed via spherical micelles. No cylindrical micelles were identified by Flodström et al.⁵³ from X-ray scattering data during SBA-15 synthesis. The suggestion about

the spherical shape of micelles in that paper⁵³ was partially based on the previously published transmission electron microscopy (TEM) data⁵⁶ showing the absence of elongated particles at the short reaction time. Note, however, that the TEM analysis was carried out under conditions very different from those employed in the paper of Flodström et al.⁵³ and in the present work. This suggests that the TEM data of the paper⁵⁶ could be hardly relevant to SBA-15 synthesis. Note that in our work the scattering patterns attributed to silica–polymer micelles after 15–25 min of syntheses I and II, which precede the appearance of the 2D hexagonal phase, cannot be fitted assuming the presence of identical spherical micelles. This discrepancy with the previous report seems to be attributed to the fact that the fitting in the paper of Flodström et al.⁵³ was limited only to the secondary scattering maxima and did not take into account the scattering behavior at very small angles near the central spot.

A more comprehensive analysis of X-ray scattering carried out in our work suggests that the cylindrical and not spherical micelles are the key intermediates of SBA-15 synthesis. The structure of cylindrical micelles has been extensively characterized in the present work during the SBA-15 synthesis using the in situ X-ray scattering data. For the 2D hexagonal phase, we have also developed the original procedure to analyze the Bragg peak intensities. This procedure allows estimation of the values of important structural parameters, the radii of the cylindrical micelles, R_1 and R_2 , and the electron densities.

A different mechanism of synthesis in a related system, a hexagonally ordered ZrO_2 /surfactant mesophase, has recently been proposed by Né et al.⁵⁹ In that case, the X-ray scattering data showed at the initial stages of the synthesis the presence of a broad “soft” peak at low q and a “sharp” Bragg peak resulting from hexagonal order. The soft peak remains in coexistence with the sharp peak and does not shift its position during the hexagonal crystallization. It was suggested⁵⁹ that the micelles act as surfactant monomer for feeding zirconia grains. The hexagonal organization proceeds on zirconia clusters which represent the nucleation sites. The mechanism proposed by Né et al.⁵⁹ is different from that observed in the present work, and the kinetic times are also much smaller (only a few seconds). Indeed, in the absence of nucleation sites introduced from the exterior (zirconia grains), the synthesis of hexagonally ordered SBA-15 appears to be initiated by packing the cylindrical surfactant template micelles coated with silica into large hexagonally ordered domains.

4. Conclusion

In situ time-resolved small-angle X-ray scattering and X-ray diffraction allow new information about the initial stages of SBA-15 synthesis to be obtained. Contrary to a previous report,⁵³ a comprehensive analysis of X-ray scattering suggests that, at the first stage of the synthesis, non-interacting cylindrical polymer–silicate micelles are formed, constituted by the poly(propylene oxide) inner core and the cylinder corona made up of a mixture of poly(ethylene oxide), water, and silicate species. At the second stage, these cylindrical micelles pack into larger domains of 2D hexagonal structure. As the synthesis proceeds, the electron density in the voids between the cylinders gradually increases as the solvent is replaced by silicate species. The volume fraction of the SBA-15 phase rapidly grows during the first 2 h of the reaction. Analysis of X-ray scattering and XRD intensities suggests that the diameters of the inner core of the cylindrical micelles and the 2D hexagonal structure do not vary much during the synthesis.

Acknowledgment. The authors acknowledge the Laboratoire pour l'Utilisation du Rayonnement Electromagnétique (L.U.R.E.), Orsay, France, for the use of the D43 experimental station for small-angle X-ray diffraction measurements. This work has been partially supported by the LURE and EC under the “Enhancing Access to Research Infrastructure” program.

References and Notes

- (1) Ryan, K. M.; Coleman, N. R. B.; Lyons, D. M.; Hanrahan, J. P.; Spalding, T. R.; Morris, M. A.; Steytler, D. C.; Heenan, R. K.; Holmes, J. D. *Langmuir* **2002**, *18*, 4996.
- (2) Corma, A. *Chem. Rev.* **1997**, *97*, 2373.
- (3) *Appl. Catal., A: Special Issue*, **2003**, 254, v.2.
- (4) Khodakov, A. Y.; Griboval-Constant, A.; Bechara, R.; Zholobenko, V. L. *J. Catal.* **2002**, *206*, 230.
- (5) Brunisma, P. J.; Hess, N. J.; Bontha, J. R.; Liu, J.; Baskaran, S. *Mater. Res. Soc. Proc.* **1997**, *443*, 105.
- (6) Esterman, M.; McCusker, L. B.; Baerlocher, C.; Merroche, A.; Kessler, H. *Nature* **1991**, *352*, 320.
- (7) Beck, J. S.; Vartuli, J. C. *Curr. Opin. Solid State Mater. Sci.* **1996**, *1*, 76.
- (8) Ying, J. Y.; Mehnert, C. P. and Wong, M. S. *Angew. Chem., Int. Ed.* **1999**, *38*, 56.
- (9) Vartuli, J. C.; Kresge, C. T.; Roth, W. J.; McCullen, S. B.; Beck, J. S.; Schmidt, K. D.; Leonowicz, M. E.; Lutner, J. D.; Sheppard, E. W. In *Advanced Catalysts and Nanostructured Materials: Modern Synthetic Methods*; Moser, W. R., Ed.; Academic Press: San Diego, CA, 1996; p 1.
- (10) Biz, S.; Occelli, M. L. *Catal. Rev.—Sci. Eng.* **1998**, *40*, 329.
- (11) Ciesla, U.; Schüth, F. *Microporous Mesoporous Mater.* **1999**, *27*, 131.
- (12) Schüth, F. *Stud. Surf. Sci. Catal.* **2001**, *135*, 1.
- (13) Zholobenko, V. L.; Evans, A. J.; Tang, S. L. Y. In *Nanoclusters and Nanocrystals*; Nalwa, H. S., Ed.; American Scientific Publishers: Stevenson Ranch, CA, 2003; pp 179–210.
- (14) Kresge, C. T.; Leonowicz, M. E.; Roth, W. J.; Vartuli, J. C.; Beck, J. S. *Nature* **1992**, *359*, 710.
- (15) Beck, J. S.; Vartuli, J. C.; Roth, W. J.; Leonowicz, M. E.; Kresge, C. T.; Schmitt, K. D.; Chu, C. T.-W.; Olson, D. H.; Sheppard, E. W.; McCullen, S. B.; Higgins, J. B.; Schlenker, J. L. *J. Am. Chem. Soc.* **1992**, *114*, 10834.
- (16) Chen, C.-Y.; Li, H.-X.; Davis, M. E. *Microporous Mater.* **1993**, *2*, 17.
- (17) Holmes, S.; Zholobenko, V.; Thursfield, A.; Plaisted, R. J.; Candy, S. C.; Dwyer, J. J. *Chem. Soc. Faraday Trans.* **1998**, *94*, 2025.
- (18) Zholobenko, V. L.; Evans, A.; Plant, D.; Holmes, S. M. *Microporous Mesoporous Mater.* **2001**, *44–45*, 793.
- (19) Zhao, D.; Feng, J.; Huo, Q.; Melosh, N.; Fredrickson, G. H.; Chmelka, B. F.; Stucky, G. D. *Science* **1998**, *279*, 548.
- (20) Zhao, D.; Sun, J.; Li, Q.; Stucky, G. D. *Chem. Mater.* **2000**, *12*, 275.
- (21) Zhao, D.; Huo, Q.; Feng, J.; Chmelka, B. F.; Stucky, G. D. *J. Am. Chem. Soc.* **1998**, *120*, 6024.
- (22) Patarin, J.; Lebeau, B.; Zana, R. *Curr. Opin. Colloid Interface Sci.* **2002**, *7*, 107.
- (23) Vartuli, J. C.; Roth, W. J.; Beck, J. S.; McCullen, S. B.; Kresge, C. T. In *Molecular Sieves: Science and Technology*; Karge, H. G., Weitkamp, J., Eds.; Springer: Heidelberg, Germany, 1998; Vol. I Synthesis, p 97.
- (24) Chen, C. Y.; Burkett, S. L.; Li, H.-X.; Davis, M. E. *Microporous Mater.* **1993**, *2*, 27.
- (25) Monnier, A.; Schuth, F.; Huo, Q.; Kumar, D.; Margolese, D.; Maxwell, R. S.; Stucky, G. D.; Krishnamurthy, M.; Petroff, P.; Firouzi, A.; Janicke, M.; Chmelka, B. F. *Science* **1993**, *261*, 1299.
- (26) Huo, Q.; Margolese, D. I.; Ciesla, U.; Feng, P.; Gier, T. E.; Sieger, P.; Leon, R.; Petroff, P.; Schuth, F.; Stucky, G. D. *Nature* **1994**, *368*, 317.
- (27) Firouzi, A.; Kumar, D.; Bull, L. M.; Besier, T.; Sieger, P.; Huo, Q.; Walker, S. A.; Zasadzinski, J. A.; Glinka, C.; Margolese, D. I.; Stucky, G. D.; Chmelka, B. F. *Science* **1995**, *267*, 1138.
- (28) Stucky, G. D.; Monnier, A.; Schuth, F.; Huo, Q.; Kumar, D.; Margolese, D. I.; Krishnamurthy, M.; Petroff, P.; Firouzi, A.; Janicke, M.; Chmelka, B. F. *Mol. Cryst. Liq. Cryst.* **1994**, *240*, 187.
- (29) Huo, Q.; Margolese, D. I.; Ciesla, U.; Demuth, P.; Feng, P.; Gier, T. E.; Sieger, P.; Firouzi, A.; Chmelka, B. F.; Schuth, F.; Stucky, G. D. *Chem. Mater.* **1994**, *6*, 1176.
- (30) Sierra, L.; Guth, J. L. *Microporous Mesoporous Mater.* **1999**, *27*, 243.

- (31) Goldsmith, I.; Von Gottberg, F. K.; Smith, K. A.; Hatton, T. A. *Langmuir* **1997**, *13*, 3659.
- (32) Nagarajan, R. *Colloids Surf., B* **1999**, *16*, 55.
- (33) Jansson, J.; Schillén, K.; Olofsson, G.; Cardoso da Silva, R.; Loh, W. *J. Phys. Chem. B* **2004**, *108*, 82.
- (34) Ruggles, J. L.; Holt, S. A.; Reynolds, P. A.; Brown, A. C.; Creagh, D. C.; White, J. W. *Phys. Chem. Chem. Phys.* **1999**, *1*, 323.
- (35) Grosso, D.; Balkenende, A. R.; Albouy, P. A.; Ayral, A.; Amenitsch, H.; Babonneau, F. *Chem. Mater.* **2001**, *13*, 1848.
- (36) Pidol, L.; Grosso, D.; Soler-Illia, G. J. A. A.; Crepaldi, E. L.; Sanchez, C.; Albouy, P. A.; Amenitsch, H.; Euzen, P. *J. Mater. Chem.* **2002**, *12*, 557.
- (37) Grosso, D.; Babonneau, F.; Albouy, P. A.; Amenitsch, H.; Balkenende, A. R.; Brunet-Bruneau, A.; Rivory, J. *Chem. Mater.* **2002**, *14*, 931.
- (38) Brennan, T.; Roser, S. J.; Mann, S.; Edler, K. J. *Langmuir* **2003**, *19*, 2639.
- (39) Pevzner, S.; Regev, O. *Microporous Mesoporous Mater.* **2000**, *38*, 413.
- (40) Gross, A. F.; Ruiz, E. J.; Le, V. H.; Tolbert, S. H. *Microporous Mesoporous Mater.* **2001**, *44–45*, 785.
- (41) Gross, A. F.; Ruiz, E. J.; Tolbert, S. H. *J. Phys. Chem. B* **2000**, *104*, 5448.
- (42) Kleitz, F.; Schmidt, W.; Schüth, F. *Microporous Mesoporous Mater.* **2001**, *44–45*, 95.
- (43) Landry, C. C.; Tolbert, S. H.; Gallis, K. W.; Monnier, A.; Stucky, G. D.; Norby, P.; Hanson, J. C. *Chem. Mater.* **2001**, *13*, 1600.
- (44) Liu, M.-C.; Sheu, H.-S.; Cheng, S. *Chem. Commun.* **2002**, 2854.
- (45) Gross, A. F.; Le, V. H.; Kirsch, B. L.; Riley, A. E.; Tolbert, S. H. *Chem. Mater.* **2001**, *13*, 3571.
- (46) Agren, P.; Linden, M.; Rosenholm, J. B.; Schwarzenbacher, R.; Kriechbaum, M.; Amenitsch, H.; Laggner, P.; Blanchard, J.; Schüth, F. *J. Phys. Chem. B* **1999**, *103*, 5943.
- (47) O'Brien, S.; Francis, R. J.; Fogg, A.; O'Hare, D.; Okazaki, N.; Kuroda, K. *Chem. Mater.* **1999**, *11*, 1822.
- (48) Rathousky, J.; Schulz-Ekloff, G.; Had, J.; Zukal, A. *Phys. Chem. Chem. Phys.* **1999**, *1*, 3053.
- (49) Linden, M.; Blanchard, J.; Schacht, S.; Schunk, S. A.; Schüth, F. *Chem. Mater.* **1999**, *11*, 3002.
- (50) Zholobenko, V. L.; Khodakov, A. Y.; Durand, D. *Microporous Mesoporous Mater.* **2003**, *66*, 297.
- (51) Impéror-Clerc, M.; Davidson, P.; Davidson, A. *J. Am. Chem. Soc.* **2000**, *122*, 11925.
- (52) Albouy, P. A.; Ayral, A. *Chem. Mater.* **2002**, *14*, 3391.
- (53) Flodström, K.; Teixeira, C. V.; Amenitsch, H.; Alfredsson, V.; Lindén, M. *Langmuir* **2004**, *20*, 4885.
- (54) Porod, G. In *Small-Angle X-ray Scattering*; Glatter O., Kratky O., Eds.; Academic Press: New York and London, 1982.
- (55) Feigin, L. A.; Svergun, D. I. In *Structure Analysis by Small-Angle X-ray and Neutron Scattering*, Taylor, G., Ed.; Plenum Press: New York and London, 1987.
- (56) Flodström, K.; Wennerström, H.; Alfredsson, V. *Langmuir* **2004**, *20*, 680.
- (57) Schmidt-Winkel, P.; Glinka, C. J.; Stucky, G. D. *Langmuir* **2000**, *16*, 356.
- (58) Guinier, A. *X-ray Diffraction: In Crystals, Imperfect Crystals and Amorphous Bodies*; Dover Publications: New York, 1994; p 103.
- (59) Né, F.; Testard, F.; Zemb, Th.; Grillo, I. *Langmuir* **2003**, *19*, 8503.